Journal of the European Ceramic Society 23 (2003) 1053–1060

www.elsevier.com/locate/jeurceramsoc

Densification of zirconia-hematite nanopowders

T.P. Raming, A.J.A. Winnubst*, W.E. van Zyl, H. Verweij[1]

Laboratory for Inorganic Materials Science, Faculty of Chemical Technology and MESA+ Research Institute, University of Twente, PO Box 217, 7500 AE Enschede, The Netherlands

Received 2 December 2001; received in revised form 3 July 2002; accepted 14 July 2002

Abstract

The densification of dual-phase yttria-doped tetragonal zirconia polycrystals (Y-TZP) and α-Fe_2O_3 (hematite) composite powders is described. Different powder synthesis methods, different forms of dry compaction processes, and two sinter methods (pressureless sintering and sinterforging) were compared. The homogeneity and average grain sizes of the sintered compacts were determined with SEM/EDX. Compacts produced from homogeneous powders that were prepared by the co-precipitation (CP) method showed large-scale phase segregation and grain growth during sintering. Compacts made from the less homogeneous sequentially precipitated (SP) powders showed far less phase segregation and relatively small grain growth during sintering. Dense (>96%) nano/nano zirconia-hematite composites were made with average grain sizes of 80 nm by sinterforging at 1000 °C and 100 MPa.

Keywords: Composites; Densification; Homogeneity; Nanocomposites; ZrO_2/α-Fe_2O_3

1. Introduction

During the mid-1980s research into the synthesis and properties of nanograined dense materials was initiated.[1] Due to size and structural effects, special properties of nanomaterials can be expected. Size effects become important if the building blocks are reduced to critical length scales of physical phenomena (e.g. the mean free paths of electrons or phonons) which can influence the electrical, magnetic and optical properties of materials. Structural effects in nanomaterials are mainly ascribed to different atomic structures of the grain boundary region compared with the bulk of the grain. A solid material containing a high density of grain boundaries has a high defect concentration. When the volume fraction of defects becomes very high, the properties of the material are influenced and change.

It can be expected that distinctive properties of nanocrystalline materials emerge in composites rather than in single-phase materials. In addition to the grain boundary components of two different kinds of grains, the variation in atomic bonding, lattice mismatches and related relaxation in the structure of the interfaces are reflected in the macroscopic properties of these composites. Nano/nano dual-phase composites in which both phases are present as grains with typical dimensions <100 nm are expected to exhibit physical properties that deviate from their coarser-grained counterparts. If one phase is electron conducting and the other electrically isolating, special properties emerge due to Schottky-barrier space-charge formation in the isolator phase near dual-phase boundaries. The extent of the Schottky-barrier (Debije length) can be of the same order as the total grain dimension resulting in special electrical properties.

The only dense (>95% from theoretical density) nano/nano ceramic oxide composites that have been reported to date are the zirconia-alumina system.[2,3] Alumina as minor phase had an inhibiting effect on the growth of zirconia grains. In cases where the alumina phase was not percolative, the growth of alumina grains was also severely retarded.[2,3] Nanograined zirconia–alumina composites had a lower hardness but increased toughness compared to larger grained zirconia–alumina composites.[4]

In order to prepare dense nano/nano composite ceramics the starting powder should not only consist of

* Corresponding author. Fax: +31-53-489-4683.
E-mail address: a.j.a.winnubst@ct.utwente.nl (A.J.A. Winnubst).
[1] Present address: Department of Materials Science and Engineering, The Ohio State University, Columbus, OH 43210-1178, USA.

0955-2219/03/$ - see front matter
PII: S0955-2219(02)00272-8

small crystallites but should also have a low degree of agglomeration.[5] One method to prepare these type of powders is to start with a single-phase powder in which the cations present in the minor phase of the final product are dissolved in the major phase. This system then transforms into a dual phase composite during sintering.[5] Another method is to start with a dual-phase powder in which the nano-crystallites of the two phases are distributed homogeneously.

This study describes the densification or sintering behaviour of nano/nano yttria-doped tetragonal zirconia (Y-TZP) and α-Fe_2O_3 (hematite) composites. The synthesis of zirconia-hematite dual-phase powders and single-phase solid solutions of iron oxide in zirconia has been described previously, using either wet-chemical techniques[6,7] or high-energy ball milling.[8] Densification of these powders has rarely been reported, however, and in most cases Fe_2O_3 was added in small amounts (up to 3 mol%) to Y-TZP in order to improve the mechanical properties of the compact.[9–11] Larger amounts of Fe_2O_3 have been added to cubic yttria-stabilised zirconia (YSZ) to probe the change in electrical and ionic conductivity of the material. In those cases formation of a dual-phase compact was reported.[12,13] Upon addition of 8 mol% $FeO_{1.5}$ to *monoclinic* zirconia followed by sintering at 1500 °C densification was improved and grain growth was inhibited by the presence of Fe^{3+} ions.[14] When 10 mol% $FeO_{1.5}$ was added to *cubic* zirconia and the powder compact was sintered at 1480 °C, densification was also improved by the presence of Fe^{3+} ions.[15] Only one investigation describes the microstructure of a dual-phase zirconia-hematite compact, where freeze-drying as powder preparation method resulted in a better homogeneity for sintered zirconia-hematite compacts compared to ball-milling.[12] This emphasises the importance of powder processing for obtaining the desired microstructure of the dual-phase zirconia/hematite composite.

The influence of the zirconia-hematite powder synthesis method and powder composition on the densification and microstructure of the resulting Y-TZP/α-Fe_2O_3 composite is described in this paper. Both single-phase solid solutions of Fe_2O_3 in zirconia and dual-phase Y-TZP/α-Fe_2O_3 powders have been prepared as starting materials to form dense composites. Different powder compaction techniques and sintering methods (pressureless sintering, sinterforging) were compared. In addition, the influence of the powder synthesis and densification parameters on the final grain size and homogeneity of the dense compact was investigated with several methods.

2. Experimental

2.1. Sample preparation

Two different synthesis routes were used to prepare powders with different compositions (Y-TZP with $FeO_{1.5}$ ranging from 27 to 43 mol%). One method was through co-precipitation (CP), in which a solution of $ZrOCl_2 \cdot 8H_2O$ (Merck), YCl_3 and $FeCl_3 \cdot 6H_2O$ (Fluka) was slowly added to an excess of concentrated (25 wt.%) ammonia (pH ~14) under vigorous stirring, resulting in immediate precipitation of mixed metal hydroxides. The second method was through a sequential precipitation (SP) method where two variations were used. In the first variation of the SP method an aqueous solution of $ZrOCl_2$ and YCl_3 was added to a basic hematite suspension. This SP method is abbreviated as SPHZ (Sequential Precipitation: first Hematite then Zirconia). For the second variation an aqueous solution of $FeCl_3$ was added to a basic suspension containing a Y-TZP powder, prepared in a way as indicated in the start of this section. This SP method is abbreviated as SPZH (Sequential Precipitation: first Zirconia then Hematite). For both SP-syntheses, the addition under vigorous stirring of the acidic metal-ion solution to concentrated (25 wt.%) ammonia (pH ~14) lead to a nucleation burst of metal hydroxides within the suspension. All (partly) amorphous gels were washed with water to remove any water-soluble species and subsequently with ethanol to remove water and disrupt hydrogen bonded networks, which otherwise led to severe aggregation upon heating. After drying at 100 °C the gels were mortared and calcined in air for 2 h at the minimum temperature necessary to obtain fully crystalline material (heating rate: 2 °C/min). This temperature varied for the different powders from 500 to 700 °C. The synthesis and characteristics of all these powders are extensively described and discussed in Ref. 16.

Single-phase 3Y-TZP (3 mol% Y_2O_3) and α-Fe_2O_3 (hematite) powders were made for comparison. These single-phase powders were made by adding aqueous solutions of either $ZrOCl_2$ and YCl_3 (to form 3Y-TZP) or $FeCl_3$ (for hematite preparation) to concentrated ammonia (pH ~14) under vigorous stirring, followed by washing of the precipitate with ethanol, drying at 100 °C and calcination at 500 °C.

Calcined powders were pressed at room temperature, using three different methods. Isostatic pressing at 400 MPa was mostly used resulting in cylindrical samples with a length of about 8 mm and a diameter of about 6 mm. A number of powder compacts were made by uniaxially pressing at 1000 MPa (UP) in a cylindrical steel mould with a diameter of 10 mm. The resulting compacts had a height of 1–2 mm. The third compaction method was magnetic pulse compaction (MPC) where a high-energy pressure wave propagates through the material. This causes large stress gradients and also adds an impulse factor resulting in an increased local pressure. The method is described extensively elsewhere.[17] The set-up generated a radial compaction field with a maximum overall pressure of 1 GPa. The resulting compacts had a diameter of 15 mm and a height of 2–3 mm.

The compacted powders were either pressureless sintered (PS) or sinterforged (SF). Pressureless sintering was performed at temperatures varying from 800 to 1250 °C for 2 h in air using a dilatometer (Netzsch 410, Germany) or a furnace (heating and cooling rates, respectively: 2 and 4 °C/min). Sinterforging of green compacts (formed through isostatic pressing) was conducted on samples which were first pressureless pre-sintered for 2 h at 850–925 °C. The resulting compacts were placed between SiC pistons and first heated to the pre-sinter temperature at a heating rate of 10 °C/min. Subsequently the samples were heated at 2 °C/min to the set temperature of 950 or 1000 °C while increasing the pressure from 0 to the final pressure (100 or 300 MPa) starting at 50 °C below set temperature. After a 25 min hold period, the pressure was decreased and the system cooled to room temperature.

2.2. Characterisation methods

The composition of powders and compacts was determined with quantitative X-Ray-Fluorescence spectrometry (XRF) using a Philips PW 1480/10-fluorometer (Eindhoven, The Netherlands). All measurements were performed in duplicate. The XRF-measurement procedure was described previously.[18]

X-ray diffraction patterns (XRD) revealed the phase composition of the compacts. XRD data were recorded on a Philips X'Pert-1 PW3710 diffractometer (Eindhoven, The Netherlands), using Cu-K_α radiation. The divergence slit was set to either 1° using a Ni-filter in the secondary (diffracted) beam or to an irradiated length of 10 mm when using a secondary curved graphite monochromator optimised for Cu-radiation. In all cases the receiving slit was set to 0.1 mm. The density of the compacts was determined by the Archimedes technique using mercury for non-dense ($<90\%$) and water for dense ($>90\%$) compacts.

The sintered compacts were investigated by Scanning Electron Microscopy (SEM). Either a Philips XL30 Environmental Scanning Electron Microscope with Field Emission Gun (Eindhoven, The Netherlands) or a Hitachi S4700 (Tokyo, Japan) was used to record Back Scatter Electron (BSE) and Secondary Electron (SE) images at different magnifications. The micrographs were used to determine the average grain size of both the zirconia and hematite phase. BSE pictures were made from polished, non-etched samples. The viewed samples were then thermally etched by heating at 30–50 °C below the sintering temperature for 15–30 min. The exact same locality on the samples that were viewed with BSE-SEM before etching was also viewed with SE-SEM after etching. The SE-graphs showed the grain boundaries between all grains, but could not be used to determine the phase of the different grains. The BSE-graphs, on the other hand, showed the phase difference but not the grain boundaries between grains of the same phase, and hence combinations of BSE- and SE- graphs of the same locality could be used to reveal all individual grains of both the Y-TZP and Fe_2O_3 phase. The average grain sizes of the two phases could then be calculated using the linear intercept method.[19]

2.3. Analysis of homogeneity

The distribution of the elements Fe and Zr within the powders and sintered compacts was probed by performing a series of EDX measurements in order to quantify the homogeneity. The powders were pressed uniaxially at 1000 MPa into cylindrical compacts of 10 mm diameter and ~3 mm in height. The density of these compacts was between 50 and 60%. The pressed powders and sintered compacts were coated with a 5 nm carbon layer to ensure electron conduction at the surface. A Hitachi S800 (Japan), equipped with a Kevex Delta Energy V dispersive X-ray analysis system was used for the EDX measurements of the pressed powders. The angle of incidence was 56° and a voltage of 15 kV was applied. On each sample a series of at least 15 EDX-measurements was performed. Each measured (micro)-locality had both a diameter and information depth of ca. 1 μm. The measured spots were chosen over the whole surface of each sample, but were not chosen totally at random in the case of the pressed powders. To avoid excessive scattering of the X-ray bundle, pores were avoided as much as possible.

The homogeneity was quantified by defining an *inhomogeneity factor I*. This inhomogeneity factor was calculated by multiplying the relative standard deviation in the Fe-content with the so-called 'Student-factor', $t_n(99)$, which in this case was 5.84.[20] The following formula for I was derived:

$$I = t_n(99)(s/Fe_{av})$$

where s is the standard deviation in Fe content, Fe_{av} is the average mol% of Fe present.

The relative standard deviation in a series of measurements on single phase Fe_2O_3/Y-TZP-doped-zirconia powder (as determined by XRD) was taken as the standard deviation of the measurement method. It was assumed that the compacts were homogeneous on the measurement scale of 1 μm^2. The standard deviation in the Fe-content (s) was calculated using the following formula:

$$s = \sqrt{s_l^2 - s_b^2}$$

s_l is the standard deviation in Fe-content in series measured on localities of 1 μm^2 and s_b is the standard deviation in Fe-content in series measured on single phase systems.

At lower *I*-values the distribution of the elements Fe and Zr is more homogeneous. The average Fe-content that resulted from the series of EDX-measurements did not deviate from the average Fe-content as determined by XRF by more than a few percent. This indicated that the series of EDX measurements were representative for the measured samples.

3. Results

3.1. Compaction and sintering

The elemental and phase compositions of the calcined powders are shown in Table 1. The number in the sample key gives the amount of $FeO_{1.5}$ in mol%. The zirconia phase of the SP-powders was purely tetragonal, while for the CP-powders also cubic zirconia was present. No monoclinic zirconia was detected. The XRD spectra of the co-precipitated powders with 27 and 34 mol% $FeO_{1.5}$ (CP27 and CP34) did not show any hematite phase, while all other powders clearly showed a two phase zirconia-hematite system after the indicated calcination treatment. All SP powders showed a zirconia as well as a hematite phase after calcination. For both type of SP powders the zirconia crystals had a size of 8 nm while the hematite crystals had an average size of 24 and 57 nm for respectively the SPZH and SPHZ powders. These crystallite size data were calculated from X-ray line broadening results and were confirmed from several TEM pictures.[16] No coating on the SP particles (e.g. an Fe_2O_3 coating on the zirconia particles in SPZH) was observed as could be expected from the experimental conditions (nucleation burst in an excess of ammonia) and as was confirmed by TEM pictures.[16]

The calcined CP42 powder was compacted by isostatic pressing (IP) at 400 MPa, uniaxial pressing (UP) at 1000 MPa and by magnetic pulse compaction (MPC). The resulting compacts were sintered pressureless in air for 2 h at maximum temperatures of 900, 1000, 1100 and 1150 °C. Densities of the sintered compacts are shown in Fig. 1. The higher pressures (1 GPa) that could be obtained with uniaxial pressing and magnetic pulse compaction resulted in higher green densities of 60 and 58% respectively compared to isostatic pressing at 400 MPa which resulted in a relative density of 49%. Compared to the IP-compact, the MPC- and UP-compacts remained at higher density with increasing sintering temperature, but at the highest sintering temperatures (1100–1150 °C) the difference was only 3%. An impressive density of 94% was obtained at a relatively low sinter temperature of 1000 °C for the MPC-compact. Further optimising of the MPC process may result in a dense (>97%) composite at the relative low sinter temperature of 1000 °C resulting in a nano/nano composite with all grain sizes <100 nm.

Table 1
Elemental and phase composition of the powders after calcination

Powder	Calcination temperature (°C)	ZrO_2 (mol%)	$YO_{1.5}$ (mol%)	HfO_2 (mol%)	$FeO_{1.5}$ (mol%)	Phases present
CP42	600	54.5	2.96	0.59	42.0	H, Z
CP34	700	62.4	3.27	0.70	33.6	Z
CP27	700	68.5	3.79	0.78	26.9	Z
SPZH42	600	55.1	2.99	0.01	41.9	H, Z
SPZH34	500	63.1	2.52	0.68	33.7	H, Z
SPZH27	500	69.1	3.79	0.02	27.0	H, Z
SPHZ43	600	53.6	2.68	0.01	43.8	H, Z
SPHZ34	525	63.3	2.58	0.01	34.1	H, Z

H = Hematite; Z = Zirconia.

Sintering results of isostatically pressed compacts that were pressureless sintered at 1150 °C or sinterforged at 950 °C and a pressure of 300 MPa (SF950-P300) or 1000 °C and 100 MPa (SF1000-P100) are summarised in Table 2. In all cases sinterforging at 1000 °C and 100 MPa led to higher densities compared to sintering pressureless in air at 1150 °C. Fig. 2 shows the pressureless sintering behaviour of isostatically pressed compacts of CP42, 3Y-TZP and Fe_2O_3 (heating rate: 2 °C/min, hold time: 2 h) at increasing temperatures.

A dense α-Fe_2O_3-compact (98%) was formed by pressureless sintering at 1000 °C while the 3Y-TZP and CP42 compacts had densities <70% at this temperature.

The fast densification of the hematite compacts was also observed when comparing the densification rates as shown in Fig. 3. The pure hematite compact started to densify at 600 °C, while the composites and 3Y-TZP only started at 700–800 °C. All zirconia-hematite composites were densified at lower temperatures compared to 3Y-TZP. At $T>900$ °C the densification rate of

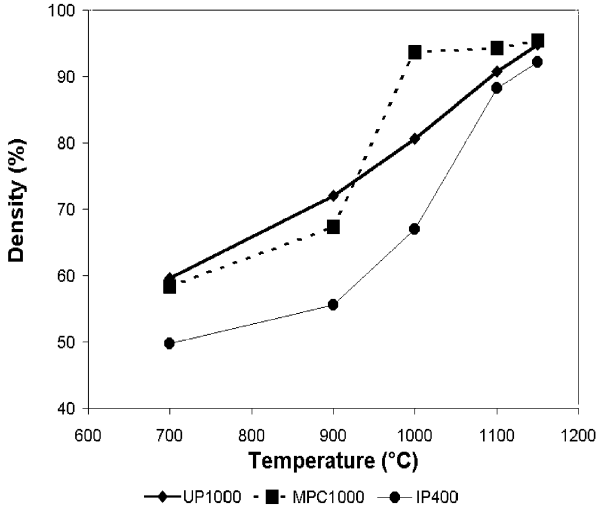

Fig. 1. Pressureless sintering of CP42 compacts. UP = Uniaxial pressing; MPC = Magnetic Pulse Compaction; IP = Isostatic Pressing.

Table 2
Relative densities of green compacts following: isostatic compaction at 400 MPa; pressureless sintering at 1150 °C (PS1150); sinterforging at 1000 °C and 100 MPa pressure (SF1000-P100); and sinterforging at 950 °C and 300 MPa pressure (SF950-P300)

	Green compact	PS1150	SF1000-P100	SF950-P300
Fe_2O_3	56	99		
CP42	50	92	97	
CP34	46	96	100	
CP27	41	93	96	
SPZH42	46	95	97	96
SPZH34	52	95	96	
SPZH27	47	98	97	
SPHZ43	47	89		
SPHZ34	47	95	98	90
3Y-TZP	49	98		

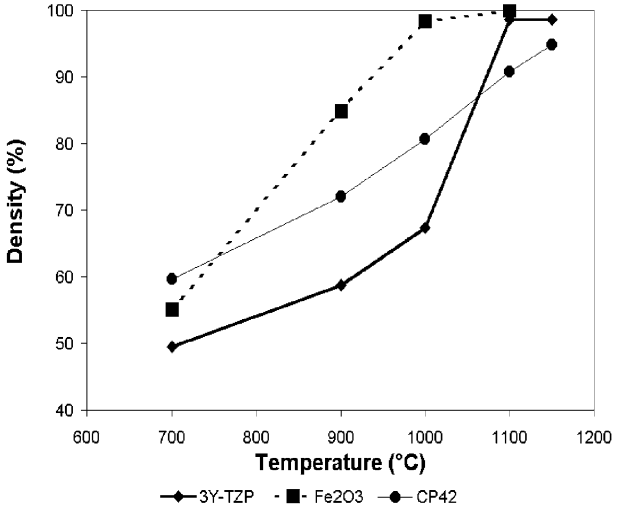

Fig. 2. Pressureless sintering of three different powder compacts as function of temperature (holding time: 2 h).

3Y-TZP, however, surpassed the densification rate of the composites, leading to higher relative densities for 3Y-TZP compacts when sintering at $T > 1000$ °C.

In Fig. 4 the densification rates of all CP-compacts are shown. The lower Fe_2O_3-containing compacts (CP27 and CP34) showed an especially strong increase in densification rate in the temperature regime of 800–900 °C, while at approximately 900 °C there was an abrupt retardation in densification. This remarkably fast low-temperature densification is described in Section 4.

3.2. Homogeneity and grain size of the sintered compacts

The inhomogeneity (I) of the Zr/Fe distribution of the sintered compacts was analysed with SEM/EDX. The inhomogeneities of the (green) powder compacts are compared with I-values of the sintered compacts and the results are shown in Table 3. The I-value increased with increasing sinter temperature for all synthesis methods and all zirconia/hematite ratios. However, I increased more rapidly with increasing sinter temperature for the CP-compacts compared to the SP-compacts. The SPHZ-compacts, on average, have about the same value for I (1.22) after pressureless sintering at 1150 °C compared to the CP-compacts (1.28), although the average I value of the SPHZ starting powders was much higher than for the CP-powders.

Sintering of the CP compacts clearly led to large-scale phase segregation and an inhomogeneous phase distribution. This phenomenon occurred to a lesser extent for the SP-compacts. The SPZH compacts show the highest homogeneity in green as well as in sintered compacts (the lowest I-values: see Table 3).

A back-scattered electron (BSE) micrograph of a SPZH42 compact after sinterforging at 1000 °C and a pressure of 100 MPa is shown in Fig. 5. The black areas on BSE graphs are hematite particles and this relatively homogeneous sample had a I value of 0.26.

A back-scattered and a secondary electron (SE) microscope picture of a sintered CP42 compact are shown in Fig. 6 which have a relatively inhomogeneous phase distribution at $I = 1.17$.

The hematite grains on the SE photos often showed flat crystal planes and straight edges. When comparing Fig. 5 with Fig. 6 it can qualitatively be observed that the hematite grains in the SPZH42 compact are more homogeneously distributed in the matrix than in the CP42 compact.

The average grain sizes of the zirconia and hematite grains in the sintered compacts are given in Table 4. Both the zirconia and hematite grains of the pressureless sintered CP-compacts are larger compared to SP-compacts, densified under similar conditions. The size of the zirconia grains of the sintered SP-compacts was smaller or equal to the size of the zirconia grains of a comparable 3Y-TZP compact, while for the CP-compacts the zirconia grains in all cases were larger than for the 3Y-TZP compact (Table 4).

The pure hematite compact sintered at 1150 °C showed much larger grains compared to the hematite grains of all zirconia-hematite composites.

The sinterforged compacts had smaller grains than the pressureless sintered compacts, which could be expected, due to the lower sintering temperature. The SPZH-compacts had the smallest grains at 1000 °C. The best result was obtained for the SPZH27 sample, which after sinterforging resulted in a dense (>97%) ceramic with the average grain size of both phases in the nano-size regime (ca. 80 nm).

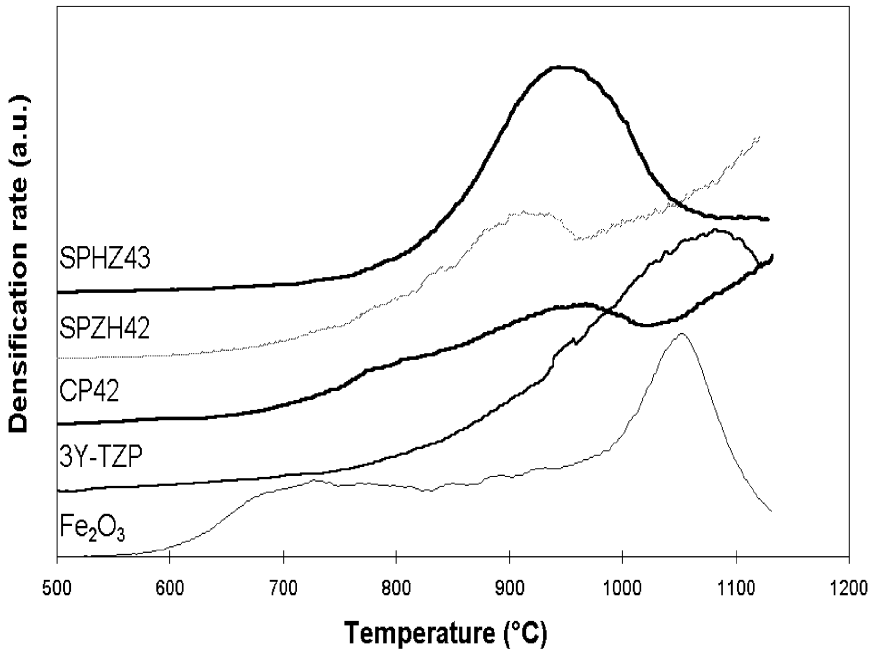

Fig. 3. Densification rates during heating (2 °C/min) of isostatically pressed compacts.

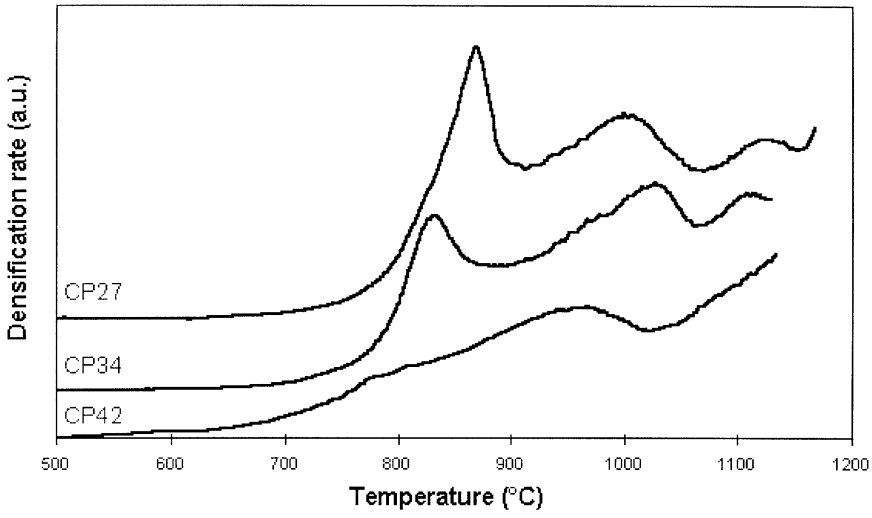

Fig. 4. Densification rates during heating (2 °C/min) of isostatically pressed co-precipitated (CP) powder compacts.

Table 3
Inhomogeneity factor of the Zr–Fe distribution (I) of powders, pressureless sintered (PS) and sinterforged (SF) compacts at temperatures (in °C) and pressures (P in MPa) as indicated

	Powders, compacted UP1000	PS1150	SF1000-P100	SF950-P300
CP42	0.28	1.17	0.63	
CP34	0	1.31	0.27	
CP27	0	1.36	0.59	
SPZH42	0.13	0.57	0.26	0.19
SPZH34	0.16	0.75	0.36	
SPZH27	0.12	0.64	0.23	
SPHZ43	0.78	1.38		
SPHZ34	0.83	1.07	0.96	

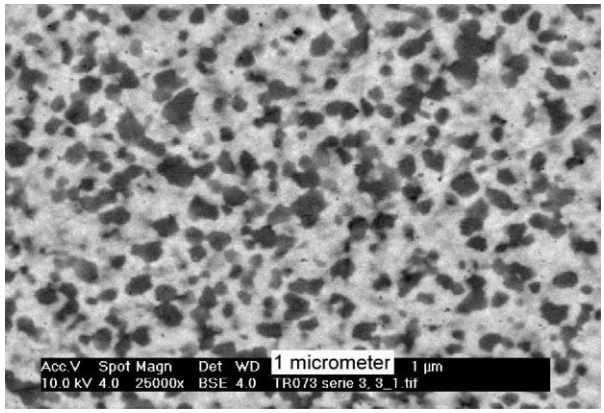

Fig. 5. Back Scattered Electron micrograph of SPZH42, sinterforged at 1000 °C and a pressure of 100 MPa (I=0.26).

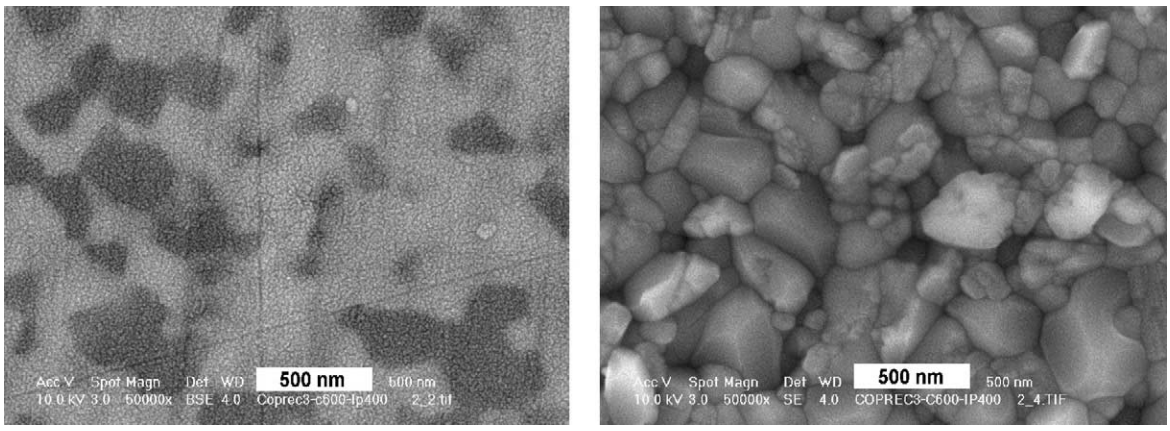

Fig. 6. Back Scattered Electron (BSE) and Secondary Electron (SE) micrographs of identical localities of a CP42 compact pressureless sintered at 1150 °C ($I = 1.17$).

Table 4
Average grain sizes (in nm) of zirconia and hematite grains after pressureless sintering at 1150 °C (PS1150) or sinter forging at 1000 °C and a pressure of 100 MPa (SF1000–100)

	PS1150		SF1000-P100	
	Zirconia	Hematite	Zirconia	Hematite
Fe_2O_3		2286		
CP42	202	294	85	137
CP34	215	358		
CP27	169	237		
SPZH42	98	218	71	102
SPZH34		305		
SPZH27	110	183	80	84
SPHZ43	122	236		
SPHZ34	75	171		
3Y-TZP	122			

4. Discussion

4.1. Compaction and sintering

For the systems investigated, pressureless sintering of isostatically pressed powders (at 400 MPa) did not lead to a nano/nano composite (grain sizes <100 nm), and it seems unlikely that this goal can be achieved with this method. By using higher pressures (e.g. by magnetic pulse compaction) during green compact formation it may be possible to obtain dense nano/nano composites after pressureless sintering these type of powders at 1000 °C. Sinter-forging, however, was more efficient in obtaining a dense nano/nano composite at this relative low temperature.

The sintering results of co-precipitated (CP) powder compacts showed a first maximum in sintering rate at a temperatures between 800 and 900 °C with the highest intensity achieved for the CP27 and CP34 compacts (see Fig. 4). This effect is explained as follows. After co-precipitation the structure of the resulting gel consisted of a zirconium hydroxide network where the Zr^{4+} ions were connected by hydroxo bridges.[21,22] In this amorphous network the Zr^{4+} ions can be readily substituted by large amounts of Y^{3+} and Fe^{3+} ions. In fully crystalline tetragonal zirconia (Y-TZP), however, only small amounts of Fe^{3+} (<1 mol%) could be dissolved in the zirconia matrix.[11] During 700 °C calcination of the CP gel, a fraction of the Fe^{3+} ions was secreted from the amorphous zirconia network while forming the crystalline zirconia phase. However, still a large percentage of Fe^{3+} ions remained dissolved in the zirconia matrix even after the calcination treatment. This amount was much higher than the expected solubility limit of Fe^{3+} in a Y-TZP matrix after sintering.[11] High-temperature X-ray powder diffraction data on all CP powders showed a change in the lattice parameter at temperatures between 700 and 900 °C.[16] A decrease in the 2θ values of the ZrO_2 (111) reflection from 30.9 to 30.3° was observed, indicating an increase in lattice parameter. This change in (111) reflection values was accompanied by an increase of the Fe_2O_3 reflection.[16] The XRD and dilatometer results indicated that at temperatures between 700 and 900 °C the relatively smaller Fe^{3+} ions were released from a 'metastable' zirconia lattice. In this temperature region, therefore, a large mobility of Fe^{3+} ions leaving the zirconia lattice was expected. This high ion-diffusivity led to a high densification rate as was observed in this temperature interval (see Fig. 4). This phenomenon also explained the stronger grain growth and dehomogenisation of CP-compacts compared to SP-compacts as discussed below.

4.2. Grain growth and homogeneity

As can be observed from Table 4 there was an intrinsic difference in grain growth behaviour between the co-precipitated (CP) and sequentially precipitated (SP) powders. A difference in homogeneity development during sintering was observed as well. The SPZH powder compacts remained the most homogeneous upon sintering, while the CP powder compacts showed the largest dehomogenisation (largest increase in I values) and the largest grain sizes after sintering at 1150 °C.

Both the larger grain size and the stronger dehomogenisation of the post-sintered CP-compacts can be explained by the excess of Fe^{3+} that diffused out of the 'metastable' zirconia lattice. This Fe^{3+} diffusion also promoted the mobility of other ions, which accelerated grain growth of the two phases and promoted dehomogenisation. Better results for obtaining a homogeneous, fine-grained (nano/nano) zirconia/hematite composite ceramic were therefore obtained by sequential precipitation of one phase in a suspension of the other phase, where the latter has the desired crystal structure.

5. Conclusions

Compacts made of *co-precipitated* zirconia-hematite powders showed the largest grain growth and phase dehomogenisation during sintering when compared to *sequentially precipitated* zirconia-hematite powders. Due to secretion of dissolved Fe^{3+} ions from a 'metastable' zirconia lattice, the ionic mobility of the whole system was increased during sintering, causing increased segregation between the two phases and grain growth within the co-precipitated compacts. A powder prepared by the SP-method where ferric hydroxide was precipitated in a suspension of crystalline zirconia (SPZH) gave the most dense zirconia-hematite dual-phase nano/nano compacts with average grain sizes for all phases between 80 and 85 nm after sinterforging at 1000 °C and 100 MPa. The SP-method in general led to the smallest grain sizes and the most homogeneous distribution between the zirconia and hematite phase. Magnetic pulse compaction offers good opportunities as dynamic powder compaction method to obtain high densities at low temperatures using pressureless sintering.

Acknowledgements

Mark Smithers is acknowledged for the EDX measurements and Herman Koster for the XRD measurements. We are indebted to Michiel Jak of the Delft University of Technology for performing the magnetic pulse compactions, Coen van Dijk of the University of Groningen for making many SEM-pictures and Dr. Schmitt of Hitachi Ratingen for the Hitachi-SEM pictures. We gratefully acknowledge the Chemical Sciences (CW) foundation of the Netherlands Organisation for Scientific Research (NWO) for financial support.

References

1. Birringer, R., Gleiter, H., Klein, H.-P. and Marquardt, P., Nanocrystalline materials: an approach to a novel solid structure with gas-like disorder?. *Phys. Lett.*, 1984, **102Z**, 365–369.
2. Sturm, A., Betz, U., Scipione, G. and Hahn, H., Grain growth and phase stability in a nanocrystalline ZrO_2-15wt% Al_2O_3 ceramic. *Nanostruct. Mater.*, 1999, **11**, 651–661.
3. Betz, U., Sturm, A., Löffler, J. F., Wagner, W., Wiedenmann, A. and Hahn, H., Microstructural development during final-stage sintering of nanostructured zirconia based ceramics. *Mater. Sci. Eng. A*, 2000, **281**, 68–74.
4. Bhaduri, S., Bhaduri, S. B. and Zhou, E., Auto ignition synthesis and consolidation of Al_2O_3-ZrO_2 nano/nano composite powders. *J. Mater. Res.*, 1998, **13**, 156–165.
5. Mayo, M. J., Processing of nanocrystalline ceramics from ultrafine particles. *Intl. Mater. Rev.*, 1996, **41**, 85–115.
6. Berry, F. J., Loretto, M. H. and Smith, M. R., Iron-zirconium oxides: an investigation of structural transformations by X-Ray diffraction, electron diffraction and iron-57 Mössbauer spectroscopy. *J. Solid State Chem.*, 1989, **83**, 91–99.
7. Štefanić, G., Musić, S., Popović, S. and Nomura, K., A study of the ZrO_2-Fe_2O_3 system by XRD, ^{57}Fe Mössbauer and vibrational spectroscopies. *J. Mol. Struct.*, 1999, **480–1**, 627–631.
8. Jiang, J. Z., Poulsen, F. W. and Morup, S., Structure and thermal stability of nanostructured iron-doped zirconia prepared by high-energy ball milling. *J. Mater. Res.*, 1999, **14**, 1343–1352.
9. Gogotski, G. A., Mechanical behaviour of yttria- and ferric oxide-doped zirconia at different temperatures. *Ceram. Int.*, 1998, **24**, 589–595.
10. Lawson, S., Gill, C. P. and Dransfield, G. P., The effects of copper and iron oxide additions on the sintering and properties of Y-TZP. *J. Mater. Sci.*, 1995, **30**, 3057–3060.
11. Boutz, M. M. R., Winnubst, A. J. A., Hartgers, F. and Burggraaf, A. J., Effect of additives on sintering and deformation of tetragonal zirconia. *J. Mater. Sci.*, 1994, **29**, 5374–5382.
12. Wilhelm, R. V. Jr. and Howarth, D. S., Iron oxide-doped yttria-stabilized zirconia ceramic: iron solubility and electrical conductivity. *Ceram. Bull.*, 1979, **58**, 228–232.
13. Neuimin, A. D., Kotlyar, A. G., Pal'guev, S. F., Strekalovskii, V. N. and Batrakov, N. A., The structure and conductivity of the ZrO_2-Y_2O_3 systems containing iron, manganese, cobalt and nickel oxides. In *Electrochemistry of Molten and Solid Electrolytes, Vol. 9*, ed. S. F. Pal'guev. , 1972, pp. 73–88.
14. Hyatt, E. P., Christensen, C. J. and Cutler, I. B., Sintering of zircon and zirconia with the aid of certain additive oxides. *Ceram. Bull.*, 1957, **36**, 307–309.
15. Radford, K. C. and Bratton, R. J., Zirconia electrolyte cells part 1. Sintering studies. *J. Mater. Sci.*, 1979, **14**, 59–65.
16. Raming, T. P., Winnubst, A. J. A. and Verweij, H., The synthesis and characterisation of mixed Y_2O_3-doped-ZrO_2 and α-Fe_2O_3 nanosized powders. *J. Mater. Chem.*, in press.
17. Jak, M. G., *Dynamic Compaction of Li-ion Battery Components and Batteries*. PhD Thesis, Delft University of Technology, Delft, The Netherlands, 1999.
18. Bos, M., Vrielink, J. A. M. and Van der Linden, W. E., Non-destructive analysis of small irregularly shaped homogeneous samples by X-Ray fluorescence spectrometry. *Anal. Chim. Acta*, 2000, **412**, 203–211.
19. Mendelson, M. I., Average grain size in polycrystalline ceramics. *J. Am. Ceram. Soc.*, 1969, **52**, 443.
20. Fritz, J. S. and Schenk, G. H., In *Quantitative Analytical Chemistry*. Allyn and Bacon, Boston, 1974.
21. Mamott, G. T., Barnes, P., Tarling, S. E., Jones, S. L. and Norman, C. J., Dynamic studies of zirconia crystallisation. *J. Mater. Chem.*, 1991, **26**, 4054–4061.
22. Huang, C., Tang, Z. and Zhang, Z., Differences between zirconium hydroxide ($Zr(OH)_4{\cdot}nH_2O$) and hydrous zirconia (ZrO_2nH_2O). *J. Am. Ceram. Soc.*, 2001, **84**, 1637–1638.